Journal of Physical Science
Vol. 37(2), 17–34, 2026

Performance Evaluation of EJ-301 Liquid Scintillators at a Neutron Source Facility for Fusion and Radiation Applications

Chawidpol Sangthong,[1] Siriyaporn Sangaroon,[1,2*] Kunihiro Ogawa,[2,3] Misako Miwa,[4] Sho Toyama,[4] Shigeo Matsuyama,[4] Sawarin Buakham,[1] Arreerat Kunkanha,[1] Apiwat Wisitsorasak,[5] Nopporn Poolyarat[6] and Mitsutaka Isobe[1,2,3]

[1]Faculty of Science, Mahasarakham University, Maha Sarakham, 44150, Thailand
[2]National Institute for Fusion Science, National Institutes of Natural Sciences, Oroshi-cho, Toki, 509-5292, Japan
[3]The Graduate University for Advanced Studies, SOKENDAI, Oroshi-cho, Toki, 509-5292, Japan
[4]Tohoku University, 6-6 Aoba, Aramaki, Sendai, 980-8579, Japan
[5]Department of Physics, King Mongkut's University of Technology Thonburi, Bangkok, 10140, Thailand
[6]Thailand Institute of Nuclear Technology (Public Organisation), Bangkok, 10900, Thailand

*Corresponding author: siriyaporn.s@msu.ac.th

Published online: 28 August 2026

To cite this article: Sangthong, C. et al. (2026). Performance evaluation of EJ-301 liquid scintillators at a neutron source facility for fusion and radiation applications. *J. Phys. Sci.*, 37(2), 17–34. https://doi.org/10.21315/jps2026.37.2.2

To link to this article: https://doi.org/10.21315/jps2026.37.2.2

ABSTRACT: Organic liquid scintillators, such as EJ-301 scintillation detector, are widely used for neutron detection owing to their excellent pulse shape discrimination (PSD) capabilities. In this work, an EJ-301 scintillation detector was characterised at the neutron source facility, the Fast Neutron Laboratory (FNL) of Tohoku University, Japan, using incident neutron energies between 2.34 MeV and 5.54 MeV. The novelty of this study lies in the systematic evaluation of neutron energies using transport of ions in matter (TRIM) simulations, which account for energy losses in the Havar foil and deuterium (D2) gas target. The measured pulse-height spectra were further validated against Monte Carlo N-Particle (MCNP) calculations that incorporated the light output function and detector resolution effects. By varying the fast component integration time, an optimal value of 26 ns was determined, yielding stable neutron–gamma ray separation with figure-of-merit values up to 1.4 at 2.5 MeVee. The results provide benchmark data on EJ-301 scintillation detector performance and practical guidance for detector characterisation, supporting applications in D–D neutron spectroscopy on the Large Helical Device (LHD), in future fusion devices for fast-ion studies and in broader areas requiring reliable neutron measurements.

Keywords: neutron/gamma ray pulse shape discrimination, Fast Neutron Laboratory, EJ-301, liquid scintillation detector, fusion

1. INTRODUCTION

Organic liquid scintillators, including NE-213, EJ-301 and BC-501A, are extensively utilised across various fields, including nuclear physics research, radiation detection, homeland security, medical imaging and environmental monitoring, due to their good pulse shape discrimination (PSD) capabilities, high light output and efficient detection of both neutrons and gamma rays.[1–3] In the field of fusion research, liquid scintillation detectors have been successfully used for fast neutrons measurement, particularly in the $^{2}D + ^{2}D \rightarrow n + ^{3}He$, where D-D neutron is produced with an energy of 2.45 MeV. These detectors are crucial for diagnosing plasma behaviour, measuring neutron flux, and assessing fusion reaction rates, thereby contributing to the understanding slowing down process of the fast-ion. Liquid scintillation detectors have been widely employed in neutron spectroscopy for major fusion experiments, including Tokamak de Fontenay-aux-Roses (TFR), Joint European Torus (JET), Frascati Tokamak Upgrade (FTU) and Experimental Advanced Superconducting Tokamak (EAST).[4–7] In early plasma experiments, neutron spectroscopy was primarily utilised as a diagnostic tool for determining the fuel-ion temperature, based on the Maxwellian energy distribution of D-D neutrons emitted from thermal plasmas. In contrast, under neutral beam injection heating, the neutron spectrum departs from a Maxwellian shape. Doppler broadening and energy shifts of D–D neutrons, distributed between approximately 2 and 3 MeV, provide direct insight into the fast-ion energy distribution generated by the injected fast ions.[8,9]

Recently, Cs_2LiYCl_6:Ce crystal with ^{7}Li enrichment (CLYC7) and liquid EJ-301 scintillation detectors have been successfully employed for neutron spectroscopy at the Large Helical Device (LHD) in Gifu, Japan. Since 2019, six neutron spectroscopy systems, referred to as compact neutron emission spectrometers (CNES) based on these detectors have been primarily utilised to investigate fast-ion energy distributions in deuterium plasmas heated by neutral beam injection. The enrichment of ^{7}Li in CLYC crystals is crucial, as it significantly suppresses the large thermal-neutron absorption cross section of ^{6}Li, thereby enhancing detector performance in fusion-relevant energy ranges. The CLYC7 detector is particularly advantageous due to its high energy resolution and its ability to directly measure neutron energy through the $^{35}Cl(n,p)^{35}S$ and $^{35}Cl(n,\alpha)^{32}P$ reactions, eliminating the need for unfolding procedures. However, due to its relatively slow scintillation decay time on the order of microseconds, the CLYC7 detector is limited to operation in plasmas with low neutron emission rates.[10–13] In contrast, the EJ-301 scintillation detector exhibits a much faster decay time in the nanosecond range, allowing its use under high neutron flux conditions. However, D–D neutrons are detected indirectly via recoil protons generated through elastic scattering, and therefore spectral unfolding is required to reconstruct the neutron energy distribution.[14–16]

Prior to installation in the LHD, the EJ-301 detectors were characterised at the Fast Neutron Laboratory (FNL), Tohoku University, Japan.[17] This characterisation was essential to ensure the detectors' performance and reliability under the specific conditions expected in the LHD. At the FNL, fast neutrons are produced using the Dynamitron accelerator, which can achieve an acceleration voltage of up to 3.0 MV and deliver a deuteron beam with a current of up to 3 μA. This accelerator enables the generation of high-quality neutron beams with precise energy control, providing an ideal environment for testing and calibrating neutron detectors like EJ-301 scintillation detector. This study focuses on the performance assessment of the EJ-301 scintillation detector at the FNL. The precise neutron energies in the FNL were calculated using the transport of ions in matter (TRIM) code.[18] Neutron and gamma ray discrimination capability using the pulse shape analysis technique was established. Additionally, the energy spectra of recoil protons in relation to light output was simulated using Monte Carlo N-Particle (MCNP) code and compared to experimental data obtained at the FNL.[19] The results provide benchmark data on liquid scintillator performance and practical guidance for their application in radiation detection techniques, which are extensively employed in nuclear physics, radiation protection and fusion diagnostics. Advances in this field include high-sensitivity neutron detectors, radionuclide detection using gamma ray spectrometry and substantial progress in neutron and photon spectrometry with organic liquid scintillators.[20,21] The structure of the paper is as follows. The characteristics of the EJ-301 scintillation detector are presented in Section 2. The experimental setup at the FNL is described in Section 3. The TRIM simulations and corresponding discussion are provided in Section 4. The neutron and gamma ray PSD capabilities are discussed in Section 5. Finally, the article concludes with a summary of the findings in Section 6.

2. THE EJ-301 SCINTILLATION DETECTOR

The EJ-301 scintillator used in this study had dimensions of one inch in both diameter and height.[22] It was paired with a photomultiplier tube (PMT) of the same size, specifically the H10580-100-01 model manufactured by Hamamatsu Photonics K.K (see Figure 1[a]).[23] This combination ensures efficient light collection and conversion, which is critical for accurate neutron detection and PSD. However, with the EJ-301 scintillator, gamma rays are measured through recoil electrons, whereas neutron detection relies on neutron-proton elastic scattering, in which only the recoiled proton energy is measurable. For recoil carbon ions produced in neutron–carbon scattering, the light yield in EJ-301 scintillator was assumed to be strongly quenched and negligible compared to that of recoil protons.[24–26] In liquid scintillators, the light output from recoil protons is quenched nonlinearly, as described by the Verbinski relation and illustrated in Figure 1(b).[24] To understand the behaviour of neutron-proton elastic scattering, the light output response function of the EJ-301 scintillator was calculated by applying the light output relationship from the V.V. Verbinski relation using MCNP code.[24] In the MCNP input setup, the incident neutron source energies were set to 2 MeV, 2.45 MeV and 3 MeV as examples. Depending on the scattering angle between the neutron and the recoiled proton, the proton's energy can vary from zero to the total energy of the incoming neutron. The correlation between the recoiled proton energy and the light output arises from this interaction (see Figure 1[b]). The light output response function generated by the MCNP simulation is displayed in Figure 1(c). Consequently, unfolding techniques such as the MAXED and GRAVEL codes are required to reconstruct measured energy spectrum.[27,28] Noted that the unfolding of the spectrum is beyond the scope of this paper.

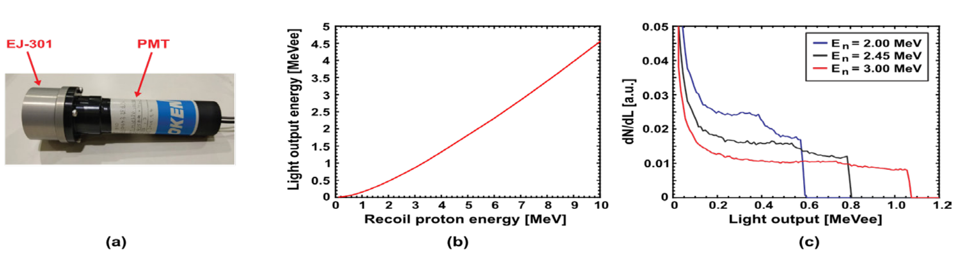

Figure 1: (a) EJ-301 scintillator coupled with a PMT; (b) Light output energy as a function of recoil-proton energy based on the V.V. Verbinski relation; (c) Example of the light output response function for different incident neutron energies, calculated using MCNP with the recoil-proton light output function taken into account.

3. THE EXPERIMENT SETUP AT FNL

Figure 2(a) shows the experimental setup in the FNL experimental hall. Note that three EJ-301 scintillation detectors were characterised, however, this study focuses on one of them, referred to as DET-1, which is discussed in detail in this article. At the FNL, five different monoenergetic neutron energies were investigated using various beam energies and detector positions at different angles relative to the beam axis, as illustrated in Figure 2(b) and detailed in Table 1. In the experiment, the detectors were operated at a voltage of –1,000 V, powered by a quad high-voltage supply, model RPH-033, manufactured by HAYASHI-REPIC Corp.[29] Signals from the detectors were sent to a fast digital data acquisition system with a sampling rate of 1 GHz and resolution of 14-bit, model APV8102-14MWPSAGb manufactured by Techno AP Corp., connected through a 1 Gbps ethernet connection.[30] Figure 2(c) presents a schematic of the electronics setup used in this study.

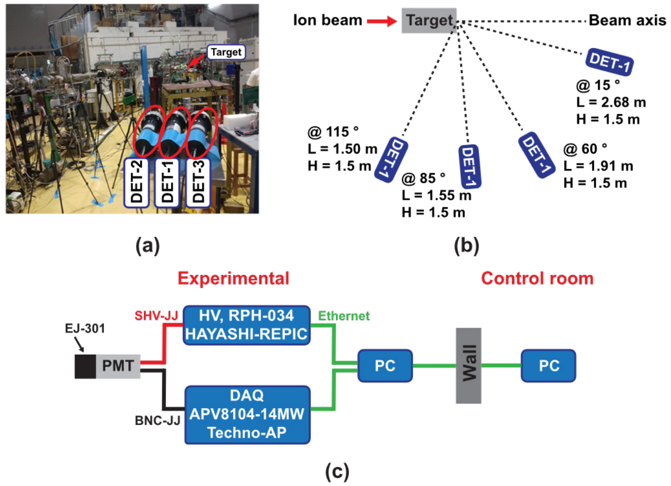

Figure 2: (a) The experimental arrangement at the FNL; (b) An overhead diagram of the experimental setup, showing the various positions of the detector. 'L' denotes the spacing between the beam target and the detector, while 'H' indicates the detector's height from the floor; (c) A schematic diagram illustrating the electronics configuration used in this experiment.

In the experiment, deuteron beams (D_{incident}) with energies of 2 MeV and 3 MeV were employed. After transmission through the Havar foil, the beams interacted with the D_2 gas (D_{gas}) target to produce neutrons. The detectors were placed at different angular positions (see Figure 2[b]) with a height of 1.5 m above the target plane. It should be noted that the detector distance in this experiment was determined by the available space around the target and was therefore neglected in the calculations. The neutron energies (E_{n}) at the detector location were simply calculated using a two-body kinematic formula for the reaction:

$$^{2}D_{incident} + {}^{2}D_{gas} \rightarrow \text{n} + {}^{3}He + 3.27 \text{ MeV} \quad (1)$$

as:

$$\sqrt{E_n} = \frac{\sqrt{M_a M_b E_a}}{M_y + M_b} cos\,\theta \pm \sqrt{\frac{M_a M_b E_a}{(M_y + M_b)^2} cos^2\theta + \frac{M_y}{M_y + M_b}\left\{Q + E_a\left(1 - \frac{M_a}{M_y}\right)\right\}} \quad (2)$$

Where, M_{a} and M_{b} are the masses of the D_{incident} and neutron, respectively, E_{a} is the incident energy of D_{incident}, M_{y} represents the mass of ^{3}He and θ represents the scattering angle. The reaction has a Q-value of 3.27 MeV. The approximate neutron energies at the detector locations in the FNL experiment, calculated using the two-body kinematic formula without accounting for attenuation in the target, are summarised in Table 1 and referred to as 'C1'. The calculation results provide an overview of the neutron energy values corresponding to different experimental configurations and detector angles.

Table 1: Five experimental configurations at the FNL, including a comparison of neutron energies at the detector positions calculated using the two-body kinematic formula without attenuation effects (C1) and with attenuation effects included via TRIM calculations (C2)

Experiment	Beam energy [MeV]	Position [Degree]	Energy [MeV]	
			C1	C2
1	3	115	2.40	2.34 ± 0.09
2	3	85	3.40	3.22 ± 0.06
3	2	60	3.95	3.47 ± 0.10
4	2	15	5.14	4.29 ± 0.09
5	3	15	6.13	5.54 ± 0.05

4. TRIM SIMULATION AND DISCUSSION

Since precise neutron energy measurement techniques, such as time-of-flight methods, were not available at the FNL, the TRIM code was employed in this work to evaluate the neutron energies at the detector. TRIM simulates the interactions of deuterons with matter—specifically the Havar foil and D_2 gas target—and provides detailed energy deposition profiles for reliable neutron energy determination. This calculation accounts for the effects of energy loss and scattering processes, allowing for an accurate determination of neutron energies based on the detector's position and experimental setup. In the initial TRIM calculation setup, the attenuation of the beam as it passed through the Havar foil and the D_2 gas target were evaluated, as illustrated in Figure 3(a). Note that the thicknesses of the Havar foil and D_2 gas target are 6.4 microns and 3 cm, respectively. The energy distribution of deuterons in the D_2 gas (E_{ion}) and the corresponding neutron energies at the detector position—taking into account the D–D cross section and two-body kinematics—were then calculated following the procedure illustrated in Figure 3(b). Before performing the calculation in D_2 gas, the transmitted beam energy after passing through the Havar foil was calculated and subsequently used as the incident beam energy for the D_2 gas target, as shown in Figure 3(c) and denoted as (1). It is clearly seen that the incident ion energies of approximately 1.24 MeV and 2.44 MeV enter the D_2 target ($E_{incident}$), corresponding to the original beam energies of 2 MeV and 3 MeV, respectively. In order to obtain the E_{ion} energy distribution in the D_2 gas, the ion energy loss (E_{loss}) as a function of depth i was evaluated using TRIM, as shown in Figure 3(d). The cumulative energy loss up to depth step i can be expressed as:

$$E_{loss}(i) = \sum_{j=1}^{i} S_j \tag{3}$$

Where, S_j is the energy loss per unit depth at step j. The deuteron energy at depth i is then given by:

$$E_{ion}(i) = E_{incident} - E_{loss}(i) \tag{4}$$

Finally, the ion energy distribution in the D_2 gas, ($Y(E)$), is obtained by interpolating $E_{ion}(i)$ and summing over all depth steps:

$$Y(E) = \sum^{i} f(E_{ion}[i]) \tag{5}$$

Where, $f(E_{ion}[i])$ represents the interpolated contribution at energy E. The resulting ion energy distribution in the D_2 gas is shown in Figure 3(e).

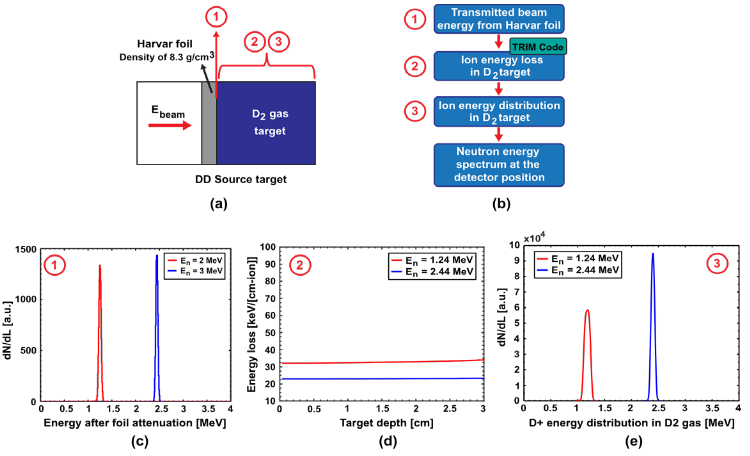

Figure 3: (a) Schematic of the Havar foil and D_2 gas target; (b) Diagram illustrating the calculation setup for the D_2 gas target and the detector location; (c) Incident ion energy distribution on the D_2 gas ($E_{incident}$); (d) Ion energy loss in the D_2 gas target (E_{loss}); (e) Ion energy distribution of deuterons in the D_2 gas target ($Y[E]$).

To calculate the neutron energy distribution at the detector positions $Y(E)$ was used as the incident deuteron energy $D_{incident}$ in Equation (1). By taking the D–D reaction cross section into account, the neutron energy at each detector position was then evaluated using the two-body kinematic formula given in Equation (2). The calculated neutron energies at the five detector positions are presented in Figure 4 and Table 1, denoted as 'C2'. As expected, because of energy losses in the Havar foil and the D_2 gas target, the neutron energies obtained from the TRIM-based calculations are lower than those derived from the two-body kinematic calculations without attenuation effects.

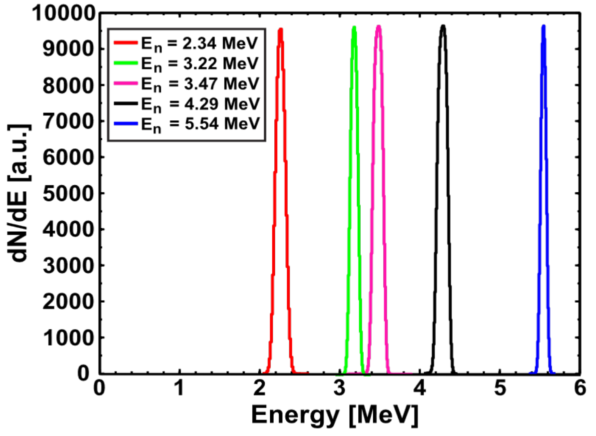

Figure 4: The calculated neutron energy spectra for the five experimental configurations are shown in Table 1.

5. CAPABILITY TO DISTINGUISH BETWEEN NEUTRON AND GAMMA RAY

Although the FNL is primarily a neutron source facility, gamma rays are generated due to inelastic neutron scattering in the surrounding structures. This additional gamma ray production is a common phenomenon in neutron facilities and can affect the measurements. The EJ-301 scintillation detector is capable of detecting both neutrons and gamma rays. In this work, the analysis focused on determining the effectiveness of PSD in differentiating between neutron and gamma ray signals. In the experiment, the digitiser waveform was recorded with a full pulse length of 64 ns. This choice was made to reflect realistic conditions for high-rate fusion experiments, such as those in the LHD, where short integration windows are often required to minimise pile-up. It should be noted that the integration length significantly affects the relative light yield of recoil protons.[31,32] Typical waveforms generated from neutrons and gamma rays, as measured with the EJ-301 detector, are depicted in Figure 5. These waveforms illustrate the detector's capability to capture and differentiate between the signals generated from neutrons and gamma rays. Although the amplitudes of the signals from both types of radiation are equal, the decay times are distinct. It is evident that the decay time of the signal generated from neutrons is longer than that generated by gamma rays. This variation in decay time is essential for distinguishing neutron signals from gamma ray signals, allowing for effective separation and accurate measurement of each type of radiation. Neutron and gamma ray signals were distinguished using the charge comparison method, which exploits their distinct decay times. The PSD parameter is defined as:

$$\text{PSD} = \frac{Q_{total} - Q_{fast}}{Q_{total}} \tag{6}$$

In the equation, Q_{total} is equal to Q_{fast} + Q_{slow}, where Q_{fast} represents the charge collected during the fast component time window (t_{fast}), and Q_{slow} represents the charge collected during the slow component time window (t_{slow}). Please note that the total integration time (t_{total}) is equal to t_{fast} + t_{slow} = 64 ns, which covers the full duration of the scintillation signal. The PSD parameter is essential for quantifying the accuracy of pulse discrimination, directly impacting the accuracy of neutron and gamma ray identification within the detector. To thoroughly investigate the neutron and gamma ray pulse shape discrimination capabilities, the t_{fast} was systematically varied between 16 ns and 32 ns. This variation allowed for the assessment of how different time windows affect the PSD and the detector's ability to accurately distinguish between neutron and gamma ray signals. In this work, values of t_{fast} below 16 ns and above 32 ns were excluded. At t_{fast} below 16 ns, neutrons and gamma rays could not be effectively discriminated. At t_{fast} above 32 ns, the PSD exhibited a very narrow band and slightly reduced values, although discrimination remained acceptable, the overall performance did not improve.

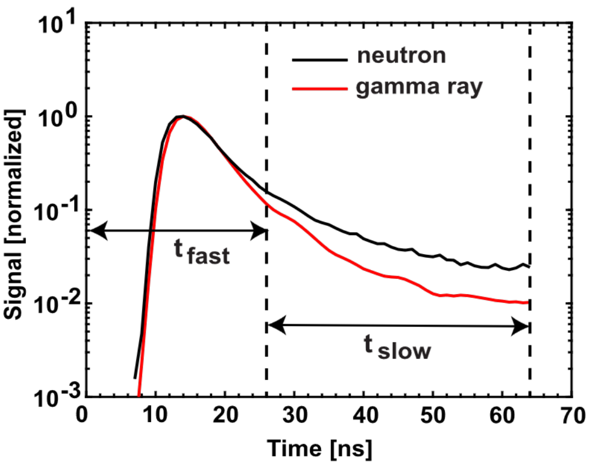

Figure 5: Typical waveforms generated from neutrons and gamma rays, as measured with the EJ-301 scintillation detector.

Figure 6 shows a PSD plot versus Q_{total} for different t_{fast} values. The example plot is taken from FNL experiment 1 in Table 1, where the neutron energy was approximately 2.34 MeV. This plot illustrates how different time windows affect the PSD values and demonstrates the detector's ability to distinguish between neutron and gamma ray. To optimise PSD performance with different time windows, the figure-of-merit (FOM) was calculated using the histogram of the PSD plot, as shown in Figure 7(a). The FOM can be calculated using the following equation:

$$\mathrm{FOM} = \frac{m_n - m_y}{\mathrm{FWHM}_n + \mathrm{FWHM}_y} \tag{7}$$

here, m_n is the peak centroids of neutron signal while m_g is the peak centroids of gamma rays signal. FWHM_n is the full-width-at-half-maximum of the neutron peak while FWHM_g is the full-width-at-half-maximum of the gamma ray peak. The FOM provides a quantitative measure of PSD performance by evaluating the separation between the neutron and gamma ray peaks relative to their respective spectral broadening. A higher FOM indicates better discrimination between neutron and gamma ray signals. Figure 7(b) shows the obtained FOM for the experiments conducted at neutron energies between 2.34 MeV and 5.54 MeV. A relatively high FOM, exceeding 1.4, was achieved when the fast component time window was set to value greater than 26 ns for the lower neutron energy of 2.34 MeV. For the higher neutron energy of 5.54 MeV, the FOM was approximately 1.

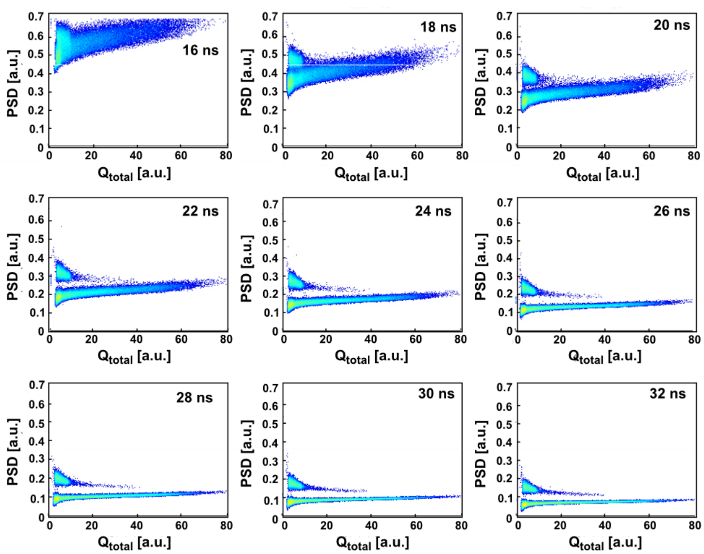

Figure 6: A 2-D plot of PSD versus Q_{total} for various t_{fast} values. This example is taken from the experiment with an incident energy of 2.34 MeV.

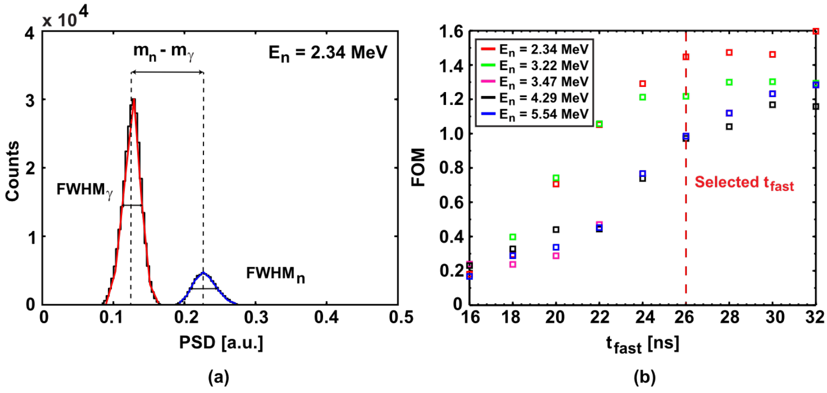

Figure 7: (a) The 2-D histogram of the PSD plot, with an example taken from the experiment where the neutron incident energy was 2.34 MeV and t_{fast} was set to 26 ns. Note that the red and blue lines represent the fitting lines; (b) Variations in the FOM value as t_{fast} varies between 16 ns and 32 ns for experiment with neutron energies ranging 2.34 MeV–5.54 MeV.

In this work, the fast component time window of 26 ns was selected for all neutron energy measurements. It was observed that FOM remained constant when the fast component time window exceeded 26 ns, indicating that further increases in the window width did not significantly enhance the discrimination between neutron and gamma ray signals. Figure 8(a)–8(e) shows a 2-D plot of the PSD versus Q_{total} with the t_{fast} set to 26 ns for measurements conducted at neutron energies of 2.34 MeV, 3.22 MeV, 3.47 MeV, 4.29 MeV and 5.54 MeV, respectively. It is evident that neutrons were effectively discriminated from gamma rays in the plot. The region-of-interest (ROI), defined by a PSD parameter above 0.172 and Q_{total} less than 40, was clearly associated with neutron signals. This indicates that the chosen fast component time window of 26 ns provided effective separation between neutron and gamma ray events, allowing for precise identification of neutron interactions in the measurements.

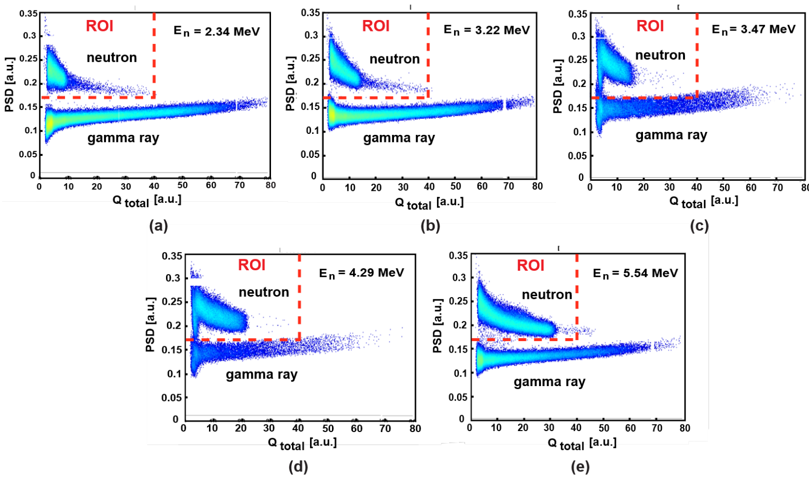

Figure 8: A 2-D plot of PSD versus Q_{total} with t_{fast} set to 26 ns for the FNL experiments with incident energies of (a) 2.3 MeV, (b) 3.22 MeV, (c) 3.47 MeV, (d) 4.29 MeV and (e) 5.54 MeV.

Figure 9(a) shows histograms of Q_{total} corresponding to neutron-induced signals in the ROI of the EJ-301 scintillation detector for measurements conducted at neutron energies of 2.34 MeV and 5.54 MeV at the FNL. To better interpret the Q_{total} histogram results, the response function of the EJ-301 scintillator to incident neutrons as a function of light output was calculated using MCNP simulations. In the MCNP simulations, the non-linear light output function for each recoil-proton, as shown in Figure 1(b), was taken into account directly in the pulse height spectrum (PHS) tally calculations. The resulting recoil-proton spectra, expressed as a function of light output (L) in electron-equivalent energy (MeVee), for the corresponding incident neutron energies are presented in Figure 9(b). Note that the response function shown in Figure 9(b) does not account for the detector's energy resolution. By performing these simulations, the observed Q_{total} distributions can be correlated with the actual energy deposition events within the detector, enabling a more precise interpretation of the data. The relationship between Q_{total} and the light output L is then determined as:

$$Q_{total}\ [\text{a.u.}] = (0.088 \times L\ [\text{MeVee}]) - 0.020 \tag{8}$$

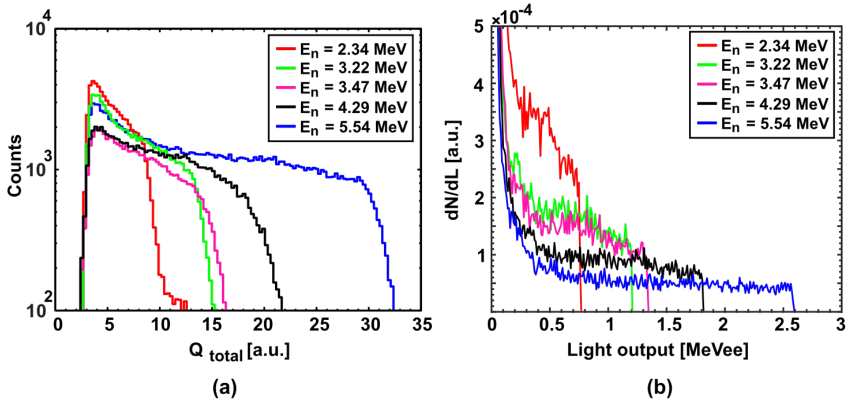

Figure 9: (a) A histogram showing the recoil-proton as a function of Q_{total}; (b) The light output function as a function of electron-equivalent energy (MeVee) for different incident neutron energies.

Furthermore, the energy resolution of the EJ-301 scintillation detector was incorporated into the calculated response function through non-linear numerical simulations, in which the experimental pulse-height spectra were matched to the simulated spectra using a non-linear least-squares fitting with an iterative reduced χ^2/ν minimisation procedure, where ν denotes the number of degrees of freedom, defined as the number of data points minus the number of fitted parameters (i.e., coefficients *a*, *b* and *c*). In the simulations, a resolution function based on a Gaussian distribution, $f(E_i)$, was convolved with the calculated response function shown in Figure 9(b). The Gaussian function is defined for the energy at step *i* as:

$$f(E_i) = A\, exp\left(-\frac{(E-E_i)^2}{2\sigma^2}\right) \tag{9}$$

Where, σ is the standard deviation of the Gaussian distribution and represents the detector resolution. The relation between $\sigma(E_i)$ and the detector resolution ($R[E_i]$) can be expressed as:

$$\sigma(E_i) = \frac{E_i \cdot R(E_i)}{2.35} = \frac{FWHM(E_i)}{2.35} = \frac{a + b\sqrt{E_i + cE_i^2}}{2.35} \tag{10}$$

Here, the coefficients *a*, *b* and *c* were determined through the non-linear least-squares fitting with iterative χ^2/υ-minimisation, in which $f(E_i)$ was folded into the response function until the calculated pulse-height spectrum (Γ) matched the experimental spectrum. The pulse-height spectrum is expressed as:

$$\Gamma = \sum^{i} f(E_i) \tag{11}$$

As an example, the Gaussian distributions across the entire energy range of the response function for an incident neutron energy of 5.54 MeV are shown in Figure 10. Note that *A* in Equation (9) was the arbitrary constant number. Using the χ^2-minimisation procedure, the optimal parameter values were determined to be: a = 0.087 ± 0.007 MeV, b = 0.148 ± 0.007 MeV$^{1/2}$ and c = 0.139 ± 0.062. This formulation allowed for a precise comparison between the experimental and simulated light output function by incorporating the energy broadening effects arising from the finite resolution of the detector (see Figure 11[a]–11[e]). The results show good agreement between the measured and calculated spectra at the spectral edge, whereas discrepancies remain at lower energies. These deviations are primarily attributed to background radiation present in the experiment, which was not included in the simulation. The quality of the agreement was quantified using the reduced χ^2, which confirms that the model adequately reproduces the main spectral features despite the low-energy discrepancies.

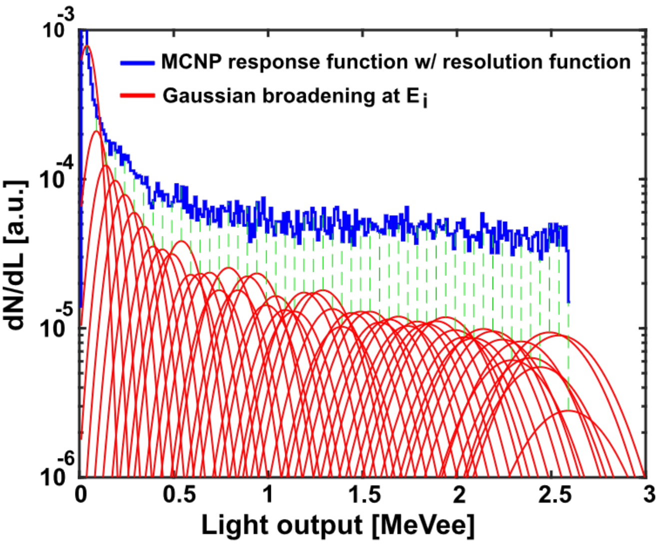

Figure 10: The convolution of a Gaussian function with the calculated response function is shown as an example for an incident neutron energy of 5.54 MeV.

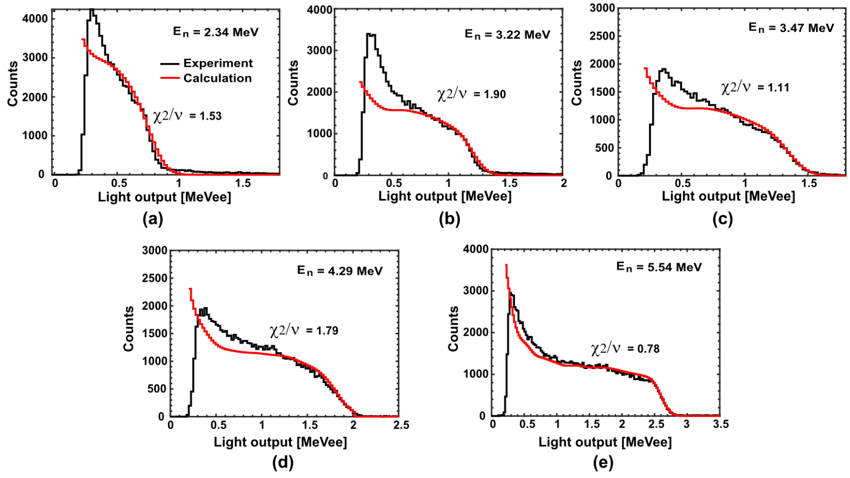

Figure 11: Comparison between the experimental and calculated pulse-height spectra.

6. CONCLUSION

In this study, the EJ-301 scintillation detector was characterised in a mixed neutron–gamma ray radiation field at the FNL. Experiments were conducted at five different fast neutron energies, with precise energy calculations performed using the TRIM code. The charge comparison method was utilised to discriminate between neutron and gamma ray signals by leveraging the differing decay times of their induced waveforms. Various time windows were optimised to enhance neutron/gamma ray discrimination, with a FOM employed to quantify the separation between these signals. The results demonstrated high neutron/gamma ray discrimination across neutron energies ranging from 2.34 MeV–5.54 MeV using a 26 ns fast component time window. Additionally, the recoil-proton pulse-height spectrum as a function of light output was compared with the calculated results, showing good agreement between experiment and simulation. This work provides benchmark performance data and a characterisation framework for EJ-301 liquid scintillators at a neutron-source-based facility, improving the reliability of compact neutron emission spectrometers. The results validate TRIM-calculated neutron spectra for experimental benchmarking and offer practical guidance for detector optimisation in mixed radiation fields. This framework can also be extended to neutron diagnostics in large fusion devices such as the LHD, future fusion devices, and broader applications requiring precise neutron–gamma discrimination.

7. ACKNOWLEDGEMENTS

This research project was financially supported by Faculty of Science, Mahasarakham University [Grant Number 6701001/2567], by Thailand Science Research and Innovation and by the National Science, Research and Innovation Fund via the Programme Management Unit for Human Resources and Institutional Development, Research and Innovation [grant number B39G670014].

8. REFERENCES

1. Perkins, L. J. & Scott, M. C. (1979). The application of pulse shape discrimination in NE213 to neutron spectrometry. *Nucl. Instrum. Methods*, 166(3), 451–464. https://doi.org/10.1016/0029-554X(79)90534-2
2. Klein, H. & Neumann, S. (2002). Neutron and photon spectrometry with liquid scintillation detectors in mixed fields. Nucl. Instrum. *Methods Phys. Res. A*, 476(1), 132–142. https://doi.org/10.1016/S0168-9002(01)01410-3
3. Klein, H. (2003). Neutron spectrometry in mixed fields: NE213/BC501A liquid scintillation spectrometers. *Radiat. Prot. Dosim.*, 107(1–3), 95–109. https://doi.org/10.1093/oxfordjournals.rpd.a006391
4. Chatelier, M., Idmtal, J., Lagattu, A. & Lepers, A. (1981). A fast neutron spectrometer for fusion experiments. *Nucl. Instrum. Methods Phys. Res.*, 190(1), 107–118. https://doi.org/10.1016/0029-554X(81)90211-1
5. Zimbal, A. et al. (2007). High resolution neutron spectrometry with liquid scintillation detectors for fusion applications. *Proceedings of the International Workshop on Fast Neutron Detectors and Applications — PoS(FNDA2006)*, 025, 035. https://doi.org/10.22323/1.025.0035
6. Kaschuck, Y. A. et al. (2002). Fast neutron spectrometry with organic scintillators applied to magnetic fusion experiments. *Nucl. Instrum. Methods Phys. Res. A*, 476(1), 511–515. https://doi.org/10.1016/S0168-9002(01)01499-1
7. Yuan, X. et al. (2013). Neutron energy spectrum measurements with a compact liquid scintillation detector on EAST. *J. Instrum.*, 8(07), P07016. https://doi.org/10.1088/1748-0221/8/07/P07016
8. Sangaroon, S. et al. (2022). Observation of significant Doppler shift in deuterium-deuterium neutron energy caused by neutral beam injection in the large helical device. *AAPPS bull.*, 32, 5. https://doi.org/10.1007/s43673-022-00036-5
9. Isobe, M. et al. (2022). Recent progress of neutron spectrometer development for LHD deuterium plasmas. *Plasma Fusion Res.*, 17, 2402008. https://doi.org/10.1585/pfr.17.2402008
10. Isobe, M. et al. (2022). Recent development of neutron and energetic-particle diagnostics for LHD deuterium discharges. *J. Instrum.*, 17(03), C03036. https://doi.org/10.1088/1748-0221/17/03/C03036

11. Sangaroon, S. et al. (2021). Neutron energy spectrum measurement using CLYC7-based compact neutron emission spectrometer in the Large Helical Device. *J. Instrum.*, 16(12), C12025. https://doi.org/10.1088/1748-0221/16/12/C12025
12. Sangaroon, S. et al. (2023). Characterization of CLYC7 scintillation detector in wide neutron energy range for fusion neutron spectroscopy. *IEEE Trans. Instrum. Meas.*, 72, 1–12. https://doi.org/10.1109/TIM.2023.3328087
13. Liao, L. Y. et al. (2024). The multi-sightline compact D–D neutron spectrometers based on CLYC7 scintillator for beam ion anisotropy study in LHD. *J. Instrum.*, 19(03), P03006. https://doi.org/10.1088/1748-0221/19/03/P03006
14. Sangaroon, S. et al. (2023). Characterization of liquid scintillator-based CNES for deuterium–deuterium neutron emission spectroscopy in the LHD. *IEEE Trans. Instrum. Meas.*, 72, 1–10. https://doi.org/10.1109/TIM.2023.3324350
15. Ogawa, K. et al. (2024). Observation of energetic ion anisotropy using neutron diagnostics in the Large Helical Device. *Nucl. Fusion*, 64(7), 076010. https://doi.org/10.1088/1741-4326/ad4909
16. Sangaroon, S. et al. (2024). Neutron spectroscopy in perpendicular neutral beam injection deuterium plasmas using newly developed compact neutron emission spectrometers. *IEEE Trans. Instrum. Meas.*, 73, 1–11. https://doi.org/10.1109/TIM.2024.3446631
17. Baba, M. et al. (1996). Development of monoenergetic neutron calibration fields between 8 keV and 15 MeV. *Nucl. Instrum. Methods Phys. Res. A*, 376(1), 115–123. https://doi.org/10.1016/0168-9002(96)00190-8
18. SRIM. (n.d.). The stopping and range of ions in matter (SRIM). Retrieved 3 May 2025, from http://www.srim.org/
19. Pelowits, D. (2013). MCNP6 user manual (Technical report, LA-CP-13-00634). Los Alamos National Laboratory, Los Alamos, NM, USA.
20. Rittirong, A. & Saenboonruang, K. (2018). Gains, uniformity and signal sharing in XY readouts of the 10 cm × 10 cm gas electron multiplier (GEM) detector. *J. Phys. Sci.*, 29(1), 121–132. https://doi.org/10.21315/jps2018.29.1.8
21. Zakaly, H. M. et al. (2019). Assessment of natural radionuclides and heavy metal concentrations in marine sediments in view of tourism activities in Hurghada City, Northern Red Sea, Egypt. *J. Phys. Sci.*, 30(3), 21–47. https://doi.org/10.21315/jps2019.30.3.3
22. Eljen Technology. (n.d.). EJ-301 & EJ-309 liquid scintillators. Retrieved May 5, 2025, from https://eljentechnology.com/products/liquid-scintillators/ej-301-ej-309
23. Hamamatsu Photonics. (n.d.). High energy PMT. Retrieved May 5, 2025, from https://www.hamamatsu.com/resources/pdf/etd/HighenergyPMT_TPMZ0003E.pdf
24. Verbinski, V. V. et al. (1968). Calibration of an organic scintillator for neutron spectrometry. *Nucl. Instrum. Methods*, 65(1), 8–25. https://doi.org/10.1016/0029-554X(68)90003-7
25. Dietze, G. & Klein, H. (1982). Gamma-calibration of NE 213 scintillation counters. *Nucl. Instrum. Methods Phys. Res.*, 193(3), 549–556. https://doi.org/10.1016/0029-554X(82)90249-X
26. Knoll, G. F. (2010). *Radiation Detection and Measurement* (4th ed.). Wiley, Hoboken.

27. Gagnon-Moisan, F. et al. (2012). Results for the response function determination of the compact neutron spectrometer. *J. Instrum.*, 7(03), C03023. https://doi.org/10.1088/1748-0221/7/03/C03023
28. Xufei, X. et al. (2012). Calibration and unfolding of the pulse height spectra of liquid scintillator-based neutron detectors using photon sources. *Plasma Sci. Technol.*, 14(6), 553. https://doi.org/10.1088/1009-0630/14/6/27
29. H-REPIC Co., Ltd. (n.d.). RPH-034: Liquid scintillation detector specifications. Retrieved 3 May 2025, from https://www.h-repic.co.jp/pdf/RPH-034.pdf
30. Techno AP Co., Ltd. (n.d.). APV8102-14MWPSA Gbe datasheet. Retrieved 3 May 2025, from http://www.techno-ap.com/img/APV8102-14MWPSAGbe.pdf
31. Brown, J. A. et al. (2018). Proton light yield in organic scintillators using a double time-of-flight technique. *J. Appl. Phys.*, 124, 045101. https://doi.org/10.1063/1.5039632
32. Laplace, T. A. et al. (2020). Scintillator light yield measurements with waveform digitizers. *Nucl. Instrum. Methods Phys. Res.*, 959(11), 163485. https://doi.org/10.1016/j.nima.2020.163485